Advanced Composites and Hybrid Materials https://doi.org/10.1007/s42114-026-01892-7

Article in Press

Nanofiber-constructed composite polymer electrolytes with dual-pathway Li transport and catalytic sulfide interfaces for lithium-sulfur batteries

Received: 2 February 2026

Accepted: 21 May 2026

Published online: 06 June 2026

Cite this article as: Kuo C., Huang W., Li J. *et al.* Nanofiber-constructed composite polymer electrolytes with dual-pathway Li transport and catalytic sulfide interfaces for lithium-sulfur batteries. *Adv Compos Hybrid Mater* (2026). https://doi.org/10.1007/s42114-026-01892-7

Chih-Yu Kuo, Wei-Ming Huang, Jing-Yu Li, Mohamed Gamal Mohamed, Shiao-Wei Kuo, Chih-Feng Huang, Bing-Joe Hwang & Yun-Sheng Ye

We are providing an unedited version of this manuscript to give early access to its findings. Before final publication, the manuscript will undergo further editing. Please note there may be errors present which affect the content, and all legal disclaimers apply.

If this paper is publishing under a Transparent Peer Review model then Peer Review reports will publish with the final article.

ARTICLE IN PRESS

© The Author(s) 2026. **Open Access** This article is licensed under a Creative Commons Attribution 4.0 International License, which permits use, sharing, adaptation, distribution and reproduction in any medium or format, as long as you give appropriate credit to the original author(s) and the source, provide a link to the Creative Commons licence, and indicate if changes were made. The images or other third party material in this article are included in the article's Creative Commons licence, unless indicated otherwise in a credit line to the material. If material is not included in the article's Creative Commons licence and your intended use is not permitted by statutory regulation or exceeds the permitted use, you will need to obtain permission directly from the copyright holder. To view a copy of this licence, visit http://creativecommons.org/licenses/by/4.0/.

ARTICLE IN PRESS

Nanofiber-Constructed Composite Polymer Electrolytes with Dual-Pathway Li^+ Transport and Catalytic Sulfide Interfaces for Lithium-Sulfur Batteries

Chih-Yu, Kuo[a], Wei-Ming Huang[a], Jing-Yu Li[a], Mohamed Gamal Mohamed[a], Shiao-Wei Kuo[a], Chih-Feng Huang[b][c], Bing-Joe Hwang[d][e], and Yun-Sheng Ye[a][e]*

[a] C. Y. Kuo, W. M. Huang, J. Y. Li, M. G. Mohamed, S. W. Kuo, Y. S. Ye

Department of Materials and Optoelectronic Science

Center of Crystal Research

National Sun Yat-Sen University

Kaohsiung 80424, Taiwan

E-mail: ysye@mail.nsysu.edu.tw

[b] Department of Chemical Engineering

i-Center for Advanced Science and Technology (iCAST)

National Chung Hsing University

Taichung 40227, Taiwan.

[c] Graduate Program in Semiconductor and Green Technology

Academy of Circular Economy

National Chung Hsing University

Nantou City, Nantou County 540216, Taiwan.

[d] B. J. Hwang

Department of Chemical Engineering

National Taiwan University of Science and Technology

Taipei 106335, Taiwan

[e] Y. S. Ye, B. J. Hwang

The Ministry of Education of Taiwan (the Sustainable Electrochemical Energy

Development Center (SEED Center) from the Featured Areas Research

Center Program

National Taiwan University of Science and Technology

Abstract

Composite polymer electrolytes (CPEs) are emerging as a promising materials platform for next-generation electrochemical systems, yet their development is often

ARTICLE IN PRESS

ARTICLE IN PRESS

constrained by insufficient mechanical integrity, limited ion-transport efficiency, and unstable interfacial chemistry in hybrid architectures. Herein, we report a nanofiber-constructed hybrid composite electrolyte formed by integrating poly(ionic liquid)-modified aramid nanofibers (PIL@ANFs) with sulfide-based lithium thiophosphate (Li_3PS_4, LPS) nanoparticles. The PIL coating stabilizes ANFs during deprotonation, preserves their nanofibrillar morphology, and enables the formation of a continuous three-dimensional Li^+ transport scaffold. Uniformly incorporated LPS nanoparticles simultaneously reinforce the mechanical framework, enhance ionic conductivity, and introduce catalytically active sulfide interfaces. The resulting hybrid composite exhibits high ionic conductivity (~10^{-3} S cm^{-1}), an elevated Li^+ transference number (>0.7), and robust interfacial stability at 60 °C. Advanced spectroscopic analyses (X-ray photoelectron spectroscopy and solid-state ^6Li nuclear magnetic resonance), combined with density functional theory and all-atom molecular dynamics simulations, reveal a dual-mode ion-transport mechanism: localized Li^+ hopping at polarized sulfide-rich domains coupled with long-range surface diffusion along the PIL@ANF network. This cooperative transport architecture also enables selective polysulfide anchoring on LPS surfaces, accelerating redox kinetics and suppressing interfacial degradation. As a proof of concept, the hybrid electrolyte enables stable lithium metal cycling and delivers high reversible capacity and rate capability in lithium–sulfur cells at elevated temperature. This work establishes a structure-guided strategy for designing mechanically robust, ionically conductive, and catalytically active hybrid composite electrolytes, highlighting the potential of nanofiber–sulfide architectures for advanced electrochemical materials.

Keyword: Hybrid composite electrolytes • Nanofiber-reinforced composites • Interfacial ion transport • Sulfide solid electrolytes • Lithium-sulfur batteries

Introduction

The global demand for sustainable and high-energy-density energy storage systems has stimulated intensive exploration of beyond Li-ion chemistries, particularly from a materials design perspective. Among these, lithium-sulfur (Li-S) batteries are highly attractive owing to their ultrahigh theoretical energy density (2600 Wh kg^{-1}) and the natural abundance of sulfur.[1] Yet, their practical implementation remains elusive, as liquid electrolyte-based Li-S cells suffer from uncontrolled polysulfide (LiPS) shuttling, sluggish redox kinetics, and intrinsically unstable electrode/electrolyte interfaces originating from the liquid-phase environment. Despite progress through functional separator design, conductive hosts, and catalytic promotion of sulfur redox,[2] liquid systems still face intrinsic safety issues such as leakage, flammability, and thermal instability. More fundamentally, these challenges highlight the limitations of liquid electrolytes as structural and functional materials in Li-S battery systems.

Solid-state electrolytes (SSEs) inherently mitigate these concerns by restricting LiPS dissolution and diffusion, suppressing lithium dendrite growth, and enhancing interfacial stability.[3, 4] However, inorganic SSEs often suffer from poor electrode

ARTICLE IN PRESS

contact and high interfacial resistance, whereas polymer electrolytes, despite their mechanical flexibility and facile processability, are constrained by modest ionic conductivity and limited electrochemical stability.[5] In parallel, significant progress has been made in the development of advanced sulfur host materials, where conductive frameworks, polar matrices, and catalytic interfaces are engineered to enhance sulfur utilization and suppress LiPS shuttling at the cathode side. [6-8] Despite these advances, such strategies are primarily confined to cathode design and do not directly address ion transport regulation and interfacial stability across the electrolyte domain. Composite polymer electrolytes (CPEs) have thus emerged as promising alternatives, in which nanoscale fillers are introduced to synergistically enhance ionic conduction and mechanical robustness. When solid ionic conductors (SICs) are employed as fillers, they provide not only intrinsic Li^+ transport pathways but also catalytic activity toward LiPS conversion, enabling concurrent enhancement of ionic kinetics and sulfur redox reactions.[9] This electrolyte-centric approach offers a complementary strategy to cathode engineering by enabling simultaneous regulation of Li^+ transport, LiPS conversion, and interfacial stability throughout the entire cell. Despite these advantages, the practical implementation of SIC-filled CPEs is severely hindered by nanoparticle agglomeration and intrinsic air/moisture sensitivity, which disrupt homogeneous dispersion, compromise interfacial integrity, and limit long-term electrochemical stability.

Sulfide-based SICs, such as Li_3PS_4, $Li_7P_3S_{11}$, and LPSCl, have recently attracted considerable attention owing to their high intrinsic ionic conductivity and their ability to catalytically mediate LiPS redox reactions.[10, 11] When integrated into polymer matrices, these sulfide fillers can synergistically couple polymer segmental motion with fast ion hopping within the sulfide lattice, thereby enabling dual regulation of bulk ion transport and interfacial redox kinetics.[12] Despite these advantages, sulfide-based SICs are highly unstable in ambient air and readily react with moisture to form Li_2S, LiOH, or H_2S,[13, 14] while their solution processing is typically restricted to low-polarity solvents to prevent chemical degradation. Collectively, these challenges hinder scalable fabrication and underscore the urgent need for rational composite designs that can stabilize sulfide fillers against air/moisture degradation, ensure homogeneous dispersion within polymer matrices, and concurrently reinforce ionic transport and mechanical integrity.

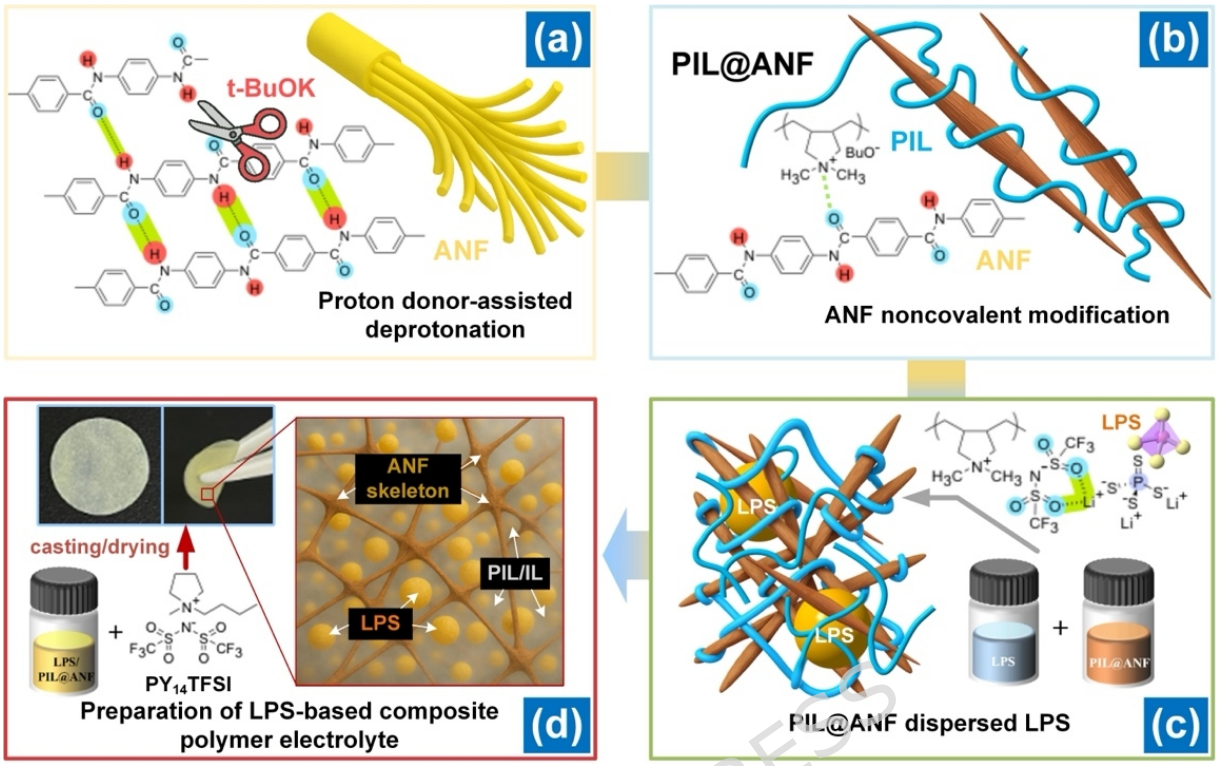

Figure 1. Schematic illustration of the fabrication of PIL@ANF/LPS CPEs: (a) deprotonation of Kevlar into ANFs; (b) PIL modification *via* noncovalent interactions; (c) uniform dispersion of LPS nanoparticles through PIL@ANF scaffolds; and (d) casting/evaporation to form a free-standing membrane, where ANFs provide mechanical strength, PIL enhances Li^+ transport, and LPS contributes both ionic conductivity and catalytic activity.

Previous strategies, including filler surface modification, porous scaffolds, and in situ polymerization approaches, [15-17] have partially alleviated nanoparticle agglomeration, yet they often involve complex processing and remain insufficient in providing robust mechanical reinforcement. Moreover, solution-based processing of sulfide electrolytes remains technically demanding because of their intrinsic solvent incompatibility and pronounced chemical instability. [18] Therefore, there is a strong demand for a facile yet effective composite framework that can simultaneously stabilize sulfide nanoparticles against degradation, ensure their homogeneous dispersion within polymer matrices, and enable the fabrication of mechanically robust, free-standing membranes.

In this work, we report a CPE based on a hierarchically integrated framework of poly(ionic liquid) (PIL)-modified aramid nanofibers (ANFs) and sulfide-based Li_3PS_4 (LPS) nanoparticles. ANFs, derived from deprotonated Kevlar, possess high tensile strength and abundant hydrogen-bonding sites (–NH and C=O), and have emerged as mechanically robust scaffolds in electrochemical systems.[19, 20] The PIL coating stabilizes ANFs during processing, preserves their nanofibrillar morphology, and functions as an ionic dispersant to enable homogeneous LPS

ARTICLE IN PRESS

distribution, while simultaneously facilitating Li^+ transport. The LPS nanoparticles contribute intrinsic ionic conductivity and act as catalytically active sites for LiPS conversion. This solution-based dispersion-evaporation strategy enables scalable fabrication of free-standing composite membranes, while simultaneously addressing nanoparticle agglomeration, mechanical fragility, and processing complexity-three persistent challenges in sulfide-based CPEs. The overall design concept is illustrated in **Figure 1**, highlighting the complementary roles of ANFs, PIL, and LPS in constructing mechanically robust and ionically efficient CPEs.

Experimental section

Preparation of Aramid Nanofiber (ANF) Dispersion. (**Figure S1**)[21] An aramid nanofiber (ANF) dispersion was prepared via base-assisted deprotonation combined with mechanical disintegration. Briefly, pretreated poly(p-phenylene terephthalamide) (PPTA, Kevlar®) fibers (3.0 g) and potassium tert-butoxide (KOtBu, 3.0 g) were added to anhydrous dimethyl sulfoxide (DMSO, 120 mL) under continuous stirring. The mixture was heated at 70 °C for 2 h, during which the fibers gradually exfoliated to form a homogeneous dark-red dispersion. The resulting ANF/DMSO solution exhibited good stability and was used directly for subsequent functionalization without further purification. The final ANF concentration was approximately 20 mg mL^{-1}.

Preparation of PIL-modified ANF (PIL@ANF). (**Figure S2**) The as-prepared ANF/DMSO dispersion was slowly added dropwise into a poly(diallyldimethylammonium chloride) (PDDA, denoted as PIL)/DMSO solution under continuous mechanical disruption using a cell disruptor, in order to overcome the strong interchain hydrogen bonding of ANFs. The mixture was maintained in an ice bath to avoid overheating. To investigate the effect of coating level, PIL/ANF weight ratios of 1:1, 3:1, and 5:1 were employed. After complete dispersion, deionized water was introduced to induce gelation of the hybrid. Excess and unbound PIL were removed by repeated washing with deionized water, yielding PIL@ANF hydrogels. Subsequently, LiTFSI was added to perform anion exchange, replacing Cl^- with $TFSI^-$. Finally, the water was removed by vacuum filtration and drying to obtain PIL@ANF($TFSI^-$) hybrids at three different coating levels (denoted as $PIL@ANF_{1@1}$, $PIL@ANF_{3@1}$, and $PIL@ANF_{5@1}$).

Preparation of PIL@ANF/IL CPE. (**Figure S3**) PIL@ANF powder was dispersed in anhydrous acetonitrile (20 mg mL^{-1}) and stirred for 2 h to form a homogeneous solution. IL was then introduced into the dispersion at three different loadings, corresponding to PIL@ANF/IL weight ratios of 1:1, 1:2, and 1:3. Each mixture was stirred continuously for 1 h to ensure uniform incorporation of IL. The resulting PIL@ANF/IL solutions were cast onto Teflon plates and dried in an oven at 60 °C for 2 h to remove the solvent. Free-standing solid-state electrolyte membranes were obtained and cut into appropriate sizes for subsequent mechanical and electrochemical tests. The samples are hereafter denoted as PIL@ANF/IL 1/1, PIL@ANF/IL 1/2, and PIL@ANF/IL 1/3, respectively.

ARTICLE IN PRESS

Preparation of NF-IL/LPS CPE. PIL@ANF powder was first dispersed in anhydrous ACN (20 mg mL^{-1}) and stirred for 2 h until a homogeneous solution was obtained. Subsequently, IL was added into the PIL@ANF dispersion at a ratio of 1:2 (PIL@ANF : IL, by weight) and stirred for an additional 1 h to ensure homogeneity. Separately, β-Li_3PS_4 (LPS) was dispersed in ACN (20 mg mL^{-1}) under ultrasonic treatment to achieve uniform dispersion. The LPS solution was then slowly introduced into the PIL@ANF/IL dispersion at different loadings (10, 20, and 30 wt.% LPS) under continuous stirring for 2 h. The resulting solution was cast onto Teflon plates and allowed to dry at ambient temperature under argon-filled glovebox conditions. After solvent evaporation, free-standing $PIL@ANF_{3@1}$/IL/LPS (denoted as NF-IL/LPS) CPEs were obtained, which were cut into appropriate sizes for subsequent electrochemical and mechanical characterization.

Structural Design and Interfacial Engineering of PIL@ANF/LPS Composite Frameworks

ANFs are characterized by strong interchain hydrogen bonding, which makes their dispersion challenging. Conventional preparation *via* strong-base (e.g., KOH, *t*-BuOK) deprotonation in DMSO followed by reprotonation generally yields micron-sized bundles with poor processability.[21] This intrinsic aggregation tendency severely restricts the use of ANFs as homogeneous scaffolds in composite electrolyte membranes. To overcome this limitation, we employed poly(diallyldimethyl ammonium) (PDDA)-based PIL as a surface modifier. PDDA, widely used to disperse graphene, BNNS, and other nanomaterials, owing to its strong electrostatic stabilization and interfacial affinity.[13] Here, the ionic PIL coating screens inter-fibrillar hydrogen bonding and introduces electrostatic repulsion, thereby stabilizing ANFs in their nanofibrillar state and preventing reaggregation. Subsequent ion exchange with LiTFSI introduced $TFSI^-$ anions, yielding PIL@ANF hybrids with markedly improved solvent compatibility. As shown in **Figure 2a**, PIL@ANF($TFSI^-$) exhibits stable and homogeneous dispersion in ACN, in sharp contrast to pristine ANFs. This solvent compatibility is critical for solution-based processing of moisture-sensitive sulfide electrolytes such as Li_3PS_4, as it enables uniform mixing while avoiding premature sulfide degradation.

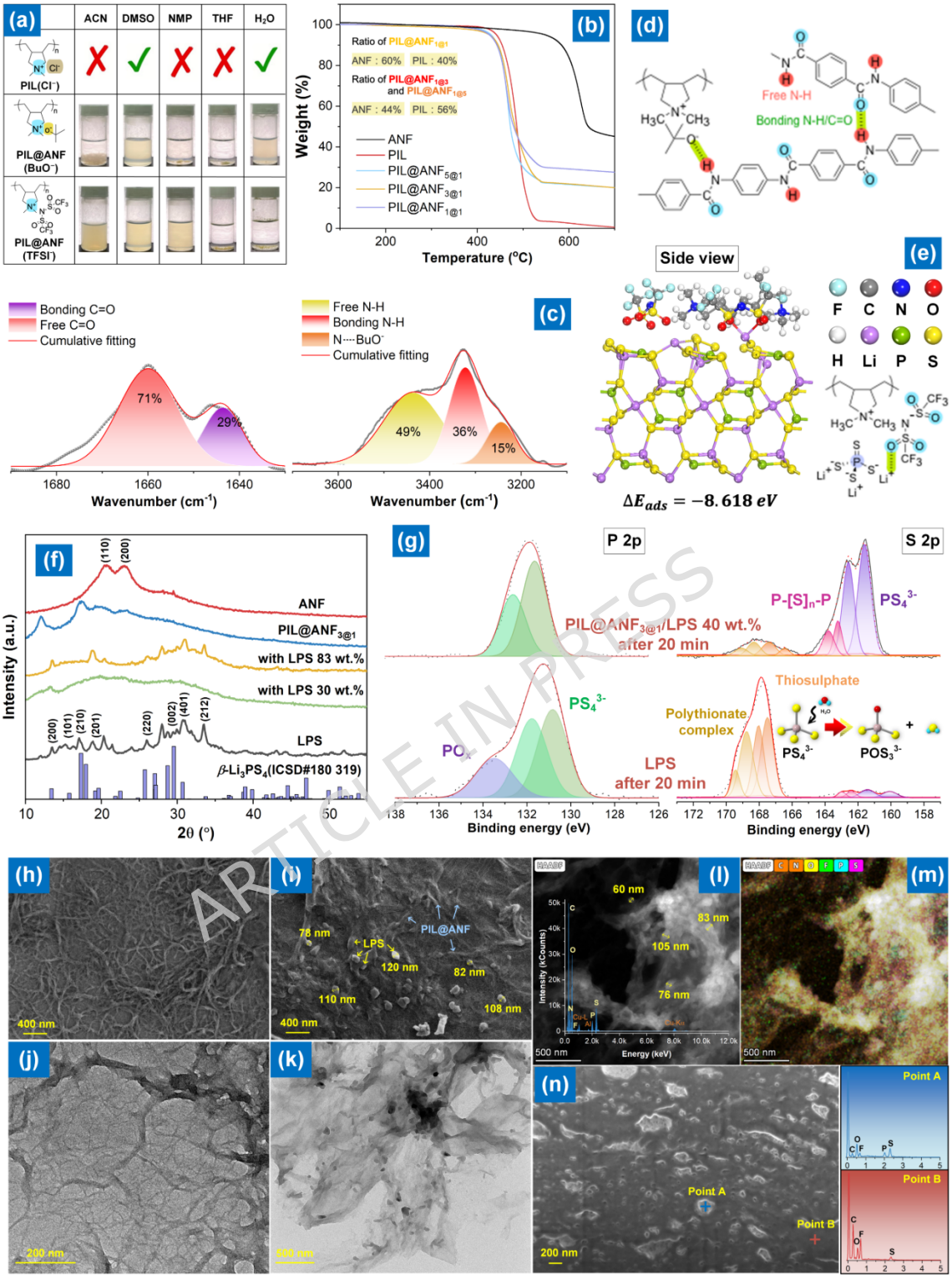

Figure 2. Structural and interfacial characterization of PIL@ANF hybrids and LPS composites. (a) Solvent compatibility of PIL@ANF hybrids. (b) TGA curves of PIL, ANF, and PIL@ANF with varied coating ratios. (c) FTIR fitting of C=O and N-H regions, and (d) schematic illustration of PIL-ANF hydrogen bonding. (e) DFT-

ARTICLE IN PRESS

optimized adsorption configuration of PIL@ANF with LPS (ΔE_{ads} = -8.618 eV). (f) XRD patterns of ANF, PIL@ANF, LPS, and PIL@ANF/LPS composites. (g) XPS P 2p and S 2p spectra before/after air exposure, highlighting improved stability of PIL@ANF-protected LPS. (h-k) SEM and TEM images of PIL@$ANF_{3@1}$ and PIL@$ANF_{3@1}$/LPS 30 wt.% hybrid, showing fibrous morphology and uniform nanoparticle dispersion. (l, m) High-resolution TEM, STEM-HAADF, and elemental mappings. (n) FIB cross-sectional SEM image of the IL-containing composite membrane with LPS and the corresponding EDS elemental mappings.

The coating content was quantified by TGA at different PDDA/ANF ratios (5:1, 3:1, 1:1). Pristine PIL decomposed completely at 700 °C, whereas ANF retained ~45% carbon residue. By comparing the residual mass, the PIL coating fraction was estimated to increase from ~40% to ~56% as the PDDA/ANF ratio increased from 1:1 to 3:1, after which no further increase was observed, indicating saturation of accessible ANF surfaces (**Figure 2b**). This saturation behavior suggests that excessive PIL does not contribute to additional interfacial coverage, but may instead lead to redundant ionic domains. FTIR spectra corroborate successful coating and ion exchange (**Figure S1**).[22] PIL@$ANF_{3@1}$ exhibited characteristic ANF amide bands (1657 cm^{-1}) and PIL C=N stretching (1510 cm^{-1}), while new peaks at 1197 and 787 cm^{-1} confirmed $TFSI^-$ incorporation. To further probe interfacial interactions, the C=O stretching region was deconvoluted (**Figure 2c**, **S2**). Compared with pristine ANF, PIL@ANF showed a higher fraction of free C=O groups, indicating effective disruption of native interchain hydrogen bonding through PIL-ANF interactions (**Figure 2d**). In parallel, analysis of the N-H stretching region revealed a free N-H band at 3438 cm^{-1} and an additional feature at 3244 cm^{-1}, assigned to N-BuO^- interactions, further supporting the formation of new ionic and hydrogen-bonding environments at the fiber interface. XPS spectra provided complementary evidence for successful surface modification (**Figure S3**). The C 1s spectrum displayed components at 285.0, 286.1, and 292.3 eV corresponding to C-C, C-N, and CF_3 species, while the N 1s region exhibited peaks at 399.4 eV (C-N-H of ANF) and 402.1 eV (quaternary N of PIL). Additional signals in the O 1s, F 1s, and S 2p regions (**Figure S4**) unambiguously confirm successful anion exchange and the presence of $TFSI^-$ within the PIL@ANF framework. Collectively, these results demonstrate that a PDDA/ANF ratio of 3:1 achieves an optimal balance between interfacial coverage and structural integrity, providing a chemically modified nanofibrous scaffold well suited for subsequent incorporation of sulfide electrolytes.

The interaction between PIL and LPS was further investigated by DFT calculations. The optimized structure (**Figure 2e**, **S5**) shows strong adsorption with an energy of -8.618 eV, suggesting a thermodynamically favorable interaction between the PIL-modified ANF surface and LPS. Such strong binding is expected to suppress nanoparticle migration and aggregation during solution processing. XRD patterns of PIL@ANF (**Figure 2f**) displayed attenuated reflections at 12.1° and 17.3°, compared with the (110) and (200) peaks of pristine ANF, attributable to disruption of interchain hydrogen bonding and reduced crystallinity induced by the amorphous PIL coating. This structural loosening is beneficial for accommodating inorganic

ARTICLE IN PRESS

fillers without compromising the continuity of the nanofibrous scaffold. Pristine β-Li_3PS_4 displayed sharp reflections at ~21°, 26°, and 28°, together with a Raman band at ~420 cm^{-1} (PS_4^{3-}, **Figure S6**).[23] These characteristic features remained visible after compositing with PIL@ANF, confirming that the crystalline structure of LPS is largely preserved. The reduced diffraction intensity is attributed to nanoscale dispersion of LPS and partial shielding by the polymeric matrix, rather than structural degradation. Air stability tests (**Figure 2g**, **S7**) further highlight the protective effect of PIL@ANF. After 20 min of air exposure, pristine LPS showed severe degradation, with S 2p signals of P=S and P-Sn-Li replaced by oxidized sulfur species, and the P 2p spectrum dominated by phosphate (Po_x). By contrast, PIL@ANF-protected LPS largely retained the P=S and P-Sn-Li signatures with only minor oxidation, demonstrating that the PIL@ANF framework acts as an effective barrier against moisture and oxygen penetration.[24] This protective effect is critical for enabling solution-based processing of sulfide electrolytes without compromising their chemical integrity.

Morphological characterization confirmed the preservation of the nanoscale fibrous structure. As shown in **Figures 2h** and **S8a**, PIL@$ANF_{3@1}$ forms a uniform one-dimensional fibrous network with diameters of 10-50 nm, comparable to pristine ANFs [25], indicating that sufficient PIL coating effectively stabilizes the nanofibrillar morphology during processing. By contrast, insufficient coating (PIL/ANF = 1:1, **Figure S9**) led to coarser and less uniform fibers, highlighting the critical role of PIL content in preventing ANF reaggregation. When hybridized with LPS, PIL@$ANF_{3@1}$ yielded composites with uniformly dispersed nanoparticles (50-120 nm, **Figures 2i** and **S8b**), while largely preserving the intrinsic particle size and morphology of pristine LPS (**Figure S10**). No obvious particle agglomeration or phase separation was observed, even at high filler loading. TEM images (**Figures 2j**, **2k**) reveal intimate interfacial contact between the fibrous scaffold and LPS domains, suggesting efficient physical confinement and interfacial interaction. Furthermore, STEM-HAADF imaging and corresponding elemental mappings (**Figures 2l-2m** and **S11**) verify the homogeneous spatial distribution of C, N, and O from the PIL@ANF framework together with P and S from LPS throughout the composite. These results collectively confirm that PIL@ANF serves as an effective nanodispersant and structural host for sulfide fillers. FIB-SEM cross-sectional imaging (**Figure 2n**) further reveals a continuous and homogeneous distribution of LPS nanoparticles across the entire membrane thickness, with no detectable aggregation or sedimentation. This observation corroborates the nanoscale dispersion identified by TEM and STEM analyses and confirms that the PIL@ANF framework effectively prevents filler clustering during solution processing.

Ion Transport and Interfacial Properties of PIL@ANF/LPS Composite Electrolytes

ARTICLE IN PRESS

The mechanical robustness of the CPEs was first evaluated by nanoindentation to assess their ability to withstand interfacial stress during cycling (**Figure 3a**). Pure PIL exhibited a low Young's modulus (7.2 MPa), whereas porous ANF prepared *via* non-solvent induced phase inversion (NIPS) [19] showed a much higher modulus (1.0 GPa), reflecting the rigid aramid backbone and strong interchain hydrogen bonding. After PIL coating, PIL@$ANF_{3@1}$ exhibited an intermediate modulus (0.3 GPa), indicating that the ionic layer softens the rigid ANF network while preserving sufficient mechanical reinforcement compared with polymer-only electrolytes. Load-displacement curves (**Figure S12**) further confirm that PIL coating effectively mitigates the intrinsic brittleness of ANFs while maintaining structural rigidity. Incorporation of rigid LPS nanoparticles further increased the modulus to 3.3-6.9 GPa,[15] evidencing efficient load transfer and strong interfacial integration between sulfide fillers and the nanofibrous scaffold. Such hierarchical mechanical reinforcement is essential for resisting Li dendrite penetration, preserving electrode-electrolyte contact, and maintaining structural integrity during prolonged electrochemical cycling.[26]

ARTICLE IN PRESS

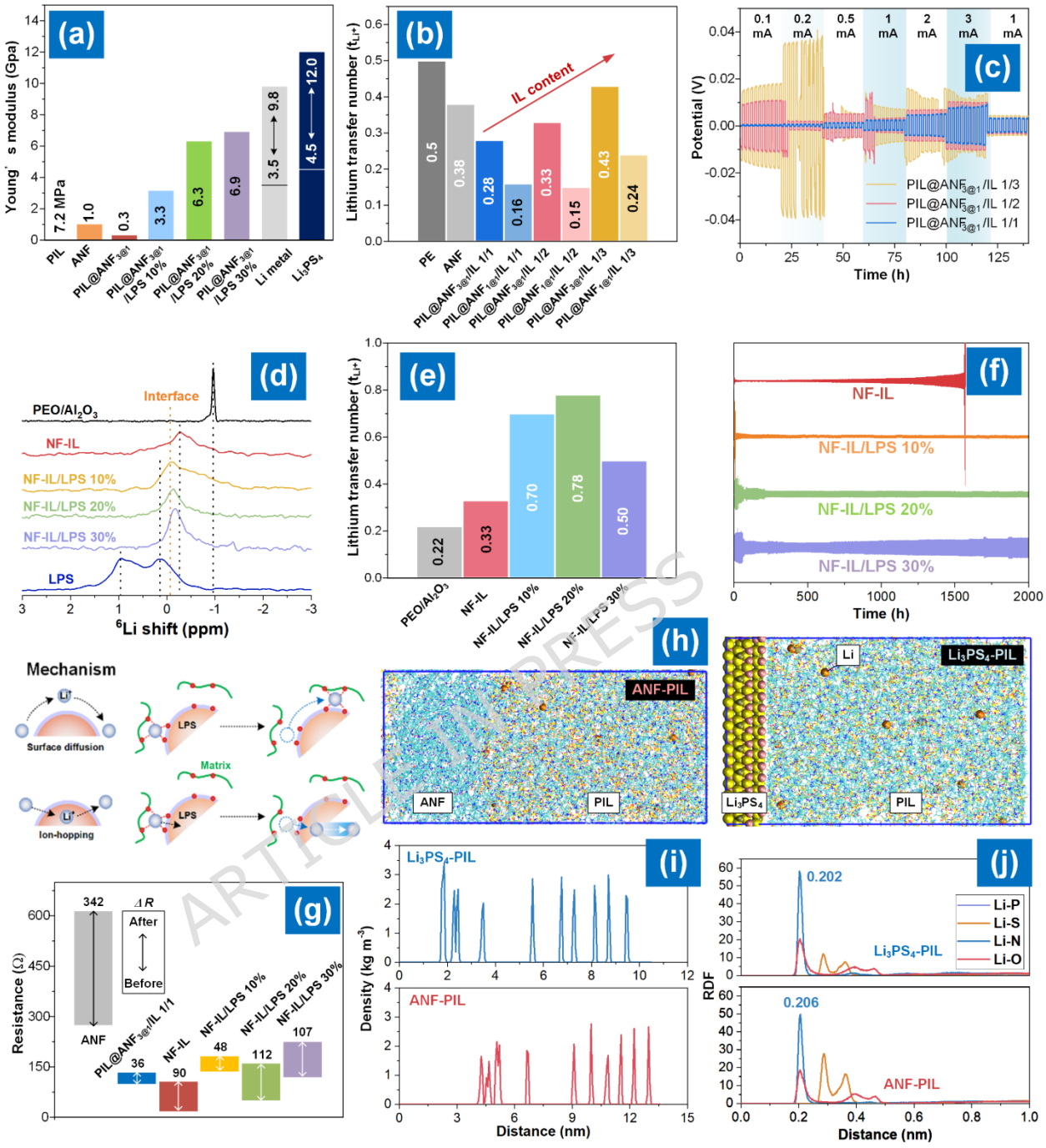

Figure 3. (a) Young's modulus of PIL, ANF, PIL@ANF$_{3@1}$, PIL@ANF$_{3@1}$/LPS, Li, and LPS from nanoindentation. (b) t_{Li^+} of PE, ANF, and PIL@ANF/IL-based CPEs. (c) Galvanostatic cycling of symmetric Li|CPE|Li cells under stepwise current densities. (d) ^{6}Li solid-state NMR spectra of PEO/Al_2O_3, NF-IL, NF-IL/LPS, and LPS with schematic Li^+ transport mechanism. (e) t_{Li^+} of PEO/Al_2O_3, NF-IL, and NF-IL/LPS CPEs. (f) Long-term Li|CPE|Li cycling at 1.0 mA cm^{-2} with NF-IL and NF-IL/LPS. (g) Interfacial resistance evolution before/after cycling. (h) Representative MD snapshots of Li^+ distribution near the PIL@ANF and Li_3PS_4-PIL interfaces. (i) Li^+

ARTICLE IN PRESS

density profiles of PIL@ANF and Li_3PS_4-PIL along the membrane normal. (j) RDF g(r) for Li-P, Li-S, Li-N, and Li-O for PIL@AFN and Li_3PS_4-PIL.

Electrochemical measurements were primarily conducted at 60 °C to enhance Li^+ transport within the polymer–IL matrix and to accelerate LiPS redox kinetics, which is also a commonly adopted condition for Li-S batteries employing solid or quasi-solid electrolytes. CPEs were fabricated by infiltrating IL into PIL-coated ANF scaffolds with different coating ratios ($PIL@ANF_{1@1}$ and $PIL@ANF_{3@1}$) and IL loadings (IL/ANF = 1/1, 1/2, and 1/3). As shown in **Figure S13**, the ionic conductivity (σ) at 60 °C increases monotonically with IL fraction, and $PIL@ANF_{3@1}$/IL consistently outperforms PIL@ANF1@1/IL, attributable to its finer and more interconnected nanofibrillar morphology that establishes a continuous three-dimensional Li^+ transport network. At comparable IL contents, PIL@ANF-based electrolytes also outperform IL-soaked PE and ANF controls, underscoring the decisive role of the charged PIL-modified framework in facilitating ion dissociation and directional Li^+ transport. To further clarify the role of the IL, a control membrane without IL was prepared and evaluated. The IL-free system exhibits a significantly lower ionic conductivity of 3.5×10^{-6} S cm^{-1} at 60 °C, nearly three orders of magnitude lower than that of the IL-containing electrolyte. This result confirms that the IL is essential for establishing an effective Li^+ transport medium. In the composite system, IL not only provides a conductive phase but also facilitates Li salt dissociation and enables the formation of continuous ion-transport pathways within the PIL@ANF framework. The Li^+ transference number at 60 °C (t_{Li^+}, **Figure 3b**), determined by polarization and electrochemical impedance spectroscopy (EIS) measurements (**Figure S14**), reaches a maximum at an intermediate IL loading (1/2), where enhanced salt dissociation and interfacial wetting are optimally balanced against excessive anion mobility. Notably, $PIL@ANF_{3@1}$/IL achieves a t_{Li^+} comparable to liquid IL separators, while preserving the mechanical integrity and safety advantages of a solid-state membrane. Symmetric Li|CPE|Li cells further validate this trend (**Figure S15**). While PE and ANF separators fail rapidly, $PIL@ANF_{3@1}$/IL electrolytes with IL loadings of 1/1 and 1/2 sustain stable Li plating/stripping for over 1000 h. Among them, the 1/1 composition exhibits the lowest overpotential, whereas the 1/2 composition offers the most balanced combination of σ, Li^+ transference number, and mechanical rigidity. Stepwise current tests (**Figure 3c**) further confirm stable operation up to 3 mA cm^{-2} for the 1/2 composition. A non-monotonic variation in overpotential is observed for IL-rich compositions (1/2 and 1/3), where the overpotential slightly decreases at higher current densities. This behavior deviates from ideal steady-state polarization and is attributed to dynamic interfacial effects. Specifically, the increased IL content enhances ionic mobility and interfacial wetting, enabling redistribution of the IL phase within the nanofibrous framework under polarization. Such reorganization can improve Li/electrolyte contact and reduce interfacial resistance at elevated current densities. Therefore, the observed decrease in overpotential reflects interfacial activation rather than intrinsic transport behavior.

ARTICLE IN PRESS

Whereas excessive IL loading (1/3) leads to rapid destabilization, likely due to compromised mechanical integrity.Whereas excessive IL loading (1/3) leads to rapid destabilization, likely due to compromised mechanical integrity. Post-mortem SEM and EIS analyses (**Figure S16**) corroborate that the 1/1 and 1/2 electrolytes maintain smooth and compact Li surfaces with only modest impedance growth, in sharp contrast to the severely degraded PE and ANF controls. Collectively, these results identify PIL@$ANF_{3@1}$/IL = 1/2 as the optimal scaffold composition, providing a mechanically robust and ionically efficient platform for subsequent incorporation of LPS fillers.

After identifying PIL@$ANF_{3@1}$/IL = 1/2 as the optimized scaffold matrix, this composition was denoted as the nanofiber-constructed IL electrolyte (NF-IL). Incorporation of LPS nanoparticles (10-30 wt.%) into NF-IL results in homogeneous dispersion throughout the matrix (**Figure S17**), with partially blurred particle boundaries arising from intimate wetting by the IL phase. Solid-state ^{6}Li NMR spectroscopy (**Figure 3d**) together with s measurements (**Figure S18**) reveal a pronounced enhancement in Li^+ transport upon LPS incorporation. The s increases progressively up to 20 wt.% LPS and shows only a slight decline at 30 wt.%, likely due to partial disruption of percolated ion-transport pathways at excessive filler loadings. Importantly, all NF-IL/LPS compositions outperform the conventional PEO/Al_2O_3 benchmark, underscoring the intrinsic advantage of sulfide-based fillers over inert oxide additives. To establish the ion-transport behavior under relevant operating conditions, temperature-dependent s measurements were performed (**Figure S19**). All samples exhibit thermally activated transport, with s increasing systematically with temperature and reaching high values at 60 °C, consistent with the electrochemical testing conditions. The Arrhenius plots yield activation energies (E_a) of 25.4, 22.0, 25.9, and 31.1 kJ mol^{-1} for NF-IL, NF-IL/LPS 10%, 20%, and 30%, respectively. The reduced E_a at 10 wt.% LPS suggests facilitated Li^+ migration upon moderate sulfide incorporation, whereas higher loadings increase the transport barrier, likely due to partial disruption of continuous ion-transport pathways. The t_{Li^+} (**Figures 3e** and **S20**), determined using the Bruce-Vincent-Evans method, should be interpreted as an apparent transference number in the presence of IL species. In such systems, ion-ion correlations and coupled ion transport can influence the measured values. Nevertheless, the observed increase in t_{Li^+} upon LPS incorporation reliably reflects enhanced Li^+-selective transport within the composite electrolyte. While NF-IL already surpasses PEO/Al_2O_3, incorporation of LPS further elevates t_{Li^+} to 0.78 at 20 wt.%, corresponding to ~3.5-fold and ~2.4-fold increases relative to PEO/Al_2O_3 (0.33) and NF-IL (0.22), respectively. This substantial enhancement highlights the dual role of sulfide fillers as both active Li^+ conductors and interfacial regulators, simultaneously promoting salt dissociation and establishing continuous Li^+ migration pathways, an effect that fundamentally exceeds the capabilities of conventional oxide additives.[27]

ARTICLE IN PRESS

The ^{6}Li solid-state NMR spectra (**Figure 3d**) provide direct insight into the Li^{+} coordination environments and transport mechanisms within the composite electrolytes. NF-IL exhibits a broad resonance centered at -0.27 ppm, characteristic of disordered Li^{+} coordination within the IL-modified nanofiber matrix,[28] whereas crystalline β-Li_3PS_4 shows two sharp resonances at 0.13 and 0.96 ppm, corresponding to Li^{+} occupying inequivalent crystallographic sites in the PS_4^{3-} framework, in agreement with previous reports.[29] Upon incorporation of LPS into NF-IL, both the broad IL-related signal and the sharp LPS-derived resonances coexist, with the intensity of the latter increasing systematically with filler loading, confirming effective integration of sulfide domains into the composite matrix. Importantly, the persistence of the broad resonance indicates dynamic Li^{+} exchange between IL-rich regions and the LPS framework, rather than phase separation, supporting a dual transport mechanism involving fast ion hopping within the sulfide lattice and surface-assisted Li^{+} diffusion along the nanofibrous scaffold. In contrast to PEO/Al_2O_3 composites, where oxide fillers primarily act as transport-inactive dispersants, NF-IL/LPS exhibits cooperative ion transport, accompanied by a resonance shift closer to 0 ppm, indicative of a less constrained Li^{+} coordination environment and more facile migration. [30] These NMR signatures highlight the intrinsic advantage of sulfide fillers in constructing highly conductive and ion-selective CPEs. Notably, although polymer-sulfide interfaces are often associated with parasitic decomposition in conventional systems,[31] the present PIL@ANF framework effectively stabilizes the sulfide domains, enabling efficient Li^{+} exchange without compromising interfacial integrity.

Electrochemical robustness was further evaluated in Li|CPE|Li symmetric cells. As shown in **Figure 3f**, NF-IL/LPS sustains stable plating/stripping for over 800 h at 1.0 mA cm^{-2} and 60 °C, markedly outperforming the LPS-free NF-IL electrolyte. EIS (**Figure 3g**) reveals significantly suppressed interfacial resistance growth upon LPS incorporation, with the 10 wt.% composite exhibiting the lowest and most stable impedance, underscoring the importance of moderate sulfide loading in maintaining interfacial integrity. Post-mortem SEM images (**Figure S21**) further corroborate this behavior, showing dense and uniform Li deposits for NF-IL/LPS, in sharp contrast to the porous and dendritic morphology observed for NF-IL. The corresponding Nyquist plots consistently confirm the stabilized interfacial characteristics. Beyond electrochemical durability, the thermal robustness of the membranes was examined (**Figure S22**). While conventional PE separators melt above 140 °C and ANF films gradually deform, all PIL@ANF/IL-based CPEs preserve their structural integrity up to 220 °C. This outstanding heat resistance originates from the rigid aramid nanofiber framework combined with the confinement of IL within the fibrous network, collectively imparting intrinsic safety to the NF-IL-based composite electrolytes.

To further elucidate the interfacial ion-transport mechanism at the molecular level, all-atom molecular dynamics (MD) simulations were conducted for the PIL@ANF and Li_3PS_4-PIL hybrid systems (**Figures 3h** and **S23**). The calculated Li^{+}

ARTICLE IN PRESS

spatial distributions reveal distinctly different coordination environments (**Figure 3i**). In the PIL@ANF system, Li^+ ions are broadly distributed along the PIL-coated nanofibers, indicative of a weakly coordinated and dynamically fluctuating ionic environment dominated by polymeric interactions. By contrast, the Li_3PS_4-PIL hybrid exhibits pronounced Li^+ accumulation near the sulfide interface, reflecting strong local polarization induced by the PS_4^{3-} units. This interfacial confinement reorganizes the first solvation shell into a hybrid coordination environment involving N, S, and O species. Radial distribution function (RDF) analysis shows that Li-N coordination remains the dominant short-range interaction in both systems; however, the first-shell Li-N peak becomes markedly sharper in the presence of Li_3PS_4 (**Figures 3j** and **S24**), indicating strengthened short-range coordination as Li^+ ions localize at the hybrid interface. Additional Li-S and Li-O contributions emerge due to the proximity of sulfide anions and framework oxygen atoms, confirming the formation of an interfacial mixed-coordination structure. Such a hybridized solvation environment is expected to facilitate localized Li^+ hopping at sulfide-rich interfaces while maintaining continuous surface diffusion along the PIL-modified nanofibers, providing a structural basis for the experimentally observed enhancement in ionic transport and interfacial stability.

ARTICLE IN PRESS

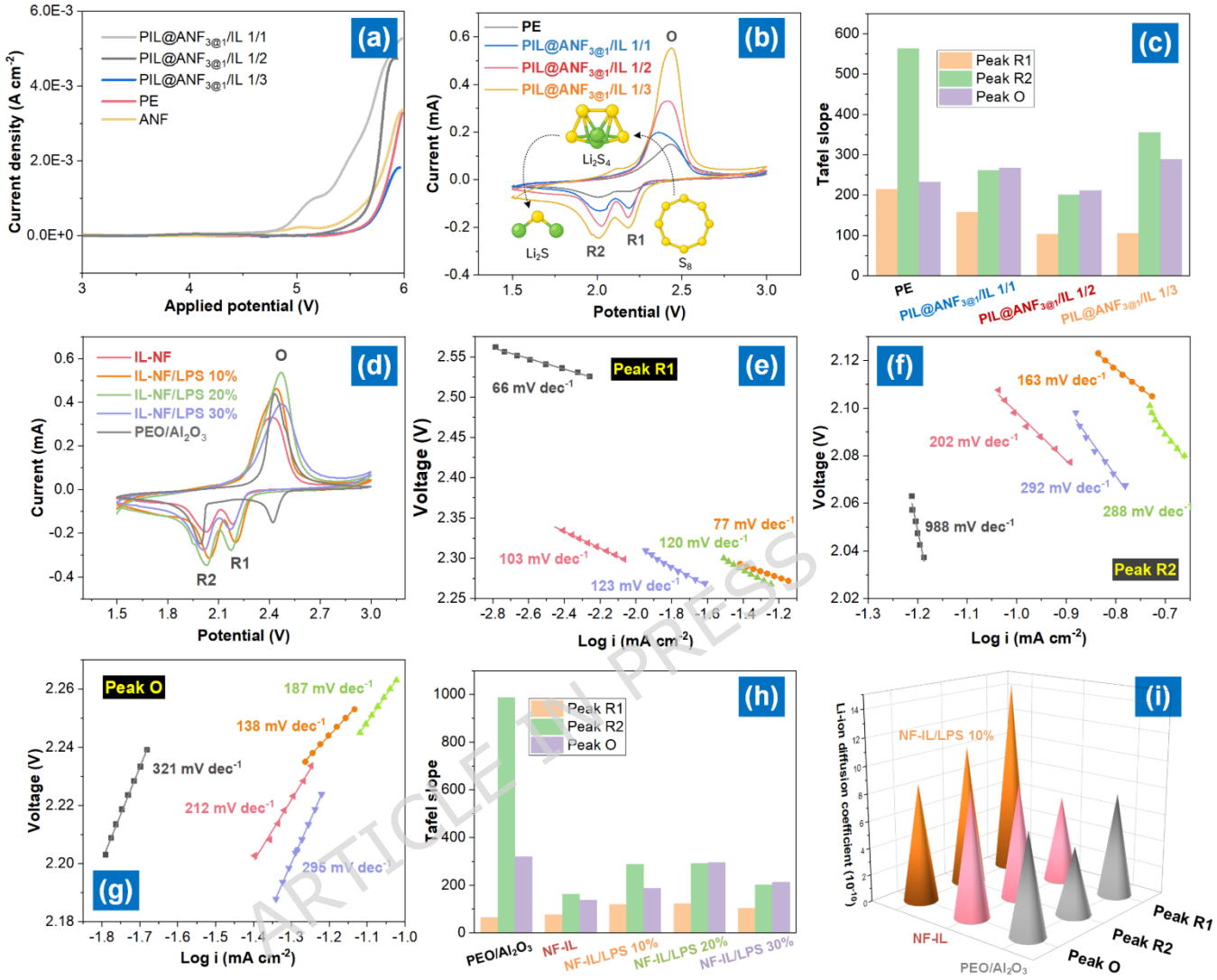

Figure 4. Electrochemical stability and catalytic activity of PIL@ANF/IL and NF-IL/LPS CPEs at 60 °C. (a) LSV curves of different CPEs showing oxidative stability. (b) CV profiles of Li-S cells with PIL@ANF/IL-based CPEs, highlighting redox peaks (O, R1, R2). (c) Corresponding Tafel slopes extracted from different peaks. (d) CV profiles of NF-IL/LPS CPEs compared with PEO/Al_2O_3. (e-g) Representative Tafel plots and slopes for peaks R1, R2, and O, respectively. (h) Comparison of Tafel slopes for NF-IL and NF-IL/LPS CPEs. (i) D_{Li^+} derived from CV analysis for different CPEs. (R1 and R2 correspond to the two-step reduction of sulfur species, while O represents the oxidation process.)

This restructured coordination environment has a direct impact on Li^+ transport behavior. Mean-squared displacement (MSD) analysis reveals that the PIL@ANF framework supports fast and continuous long-range Li^+ diffusion, whereas the LPS-PIL system shows suppressed long-range motion but retains pronounced localized

ARTICLE IN PRESS

hopping, characteristic of sulfide-assisted interfacial conduction (**Figure S25**). Importantly, in the final composite electrolyte, a three-dimensional PIL@ANF/LPS hybrid network is established, enabling the coexistence of both transport modes: (i) long-range Li^+ migration along the PIL-modified nanofiber framework and (ii) localized hopping across LPS-rich interfacial domains. In addition, the incorporated IL remains molecularly mixed with the PIL matrix rather than forming a separate phase, generating a homogeneous ionic environment that stabilizes charge carriers and facilitates Li^+ dissociation. Together, the combination of PIL-IL-enabled bulk mobility and LPS-assisted interfacial hopping constitutes a dual-pathway conduction mechanism, providing a structural and dynamical basis for the enhanced σ and interfacial stability observed experimentally.

The electrochemical stability of the PIL@ANF/IL CPEs was evaluated by linear sweep voltammetry (LSV) using a SS/CPE/SS configuration (**Figure 4a**). The results suggest a wide electrochemical stability range up to 5.5-6.0 V. It should be noted that this measurement primarily reflects the intrinsic electrochemical stability of the electrolyte, while the practical stability window in full cells may be influenced by electrode-electrolyte interfacial reactions. Similar configurations have also been reported for evaluating intrinsic electrolyte stability in polymer-based systems. Herein, the cathode composition employed in this study differs from conventional liquid-electrolyte-based systems. In the absence of liquid electrolyte infiltration, the polymer component serves not only as a binder but also as an ion-conducting matrix to enable Li^+ transport within the cathode. Therefore, a relatively high polymer content is required to maintain continuous ionic pathways and stable electrochemical operation. Similarly, the incorporation of LiTFSI is essential to ensure sufficient ionic conductivity throughout the solid-state cathode composite. While such a composition may reduce the overall energy density, it provides a necessary platform for evaluating electrolyte-cathode interfacial behavior in solid-state Li-S systems. Cyclic voltammetry (CV) conducted at 60 °C (**Figures 4b** and **S26**) reveals well-defined cathodic peaks (R1, R2) and an anodic peak (O), corresponding to the stepwise conversion of $S_8 \rightarrow Li_2S_6/Li_2S_4 \rightarrow Li_2S$. With increasing IL content, both the peak intensity and sharpness progressively improve, consistent with the enhanced σ (**Figure S13**) that facilitates LiPS redox kinetics. Among the investigated compositions, PIL@$ANF_{3@1}$/IL 1/2 (denoted NF-IL) exhibits the most balanced electrochemical response, combining pronounced redox features with moderate polarization. This behavior indicates an optimized trade-off between ion transport efficiency and interfacial reaction kinetics within the confined IL-nanofiber framework.

To elucidate the charge-transfer kinetics and clarify the role of sulfide fillers, the CV responses of NF-IL and NF-IL/LPS CPEs were directly compared (**Figure 4d**). Upon incorporation of LPS, the redox peaks exhibit markedly higher current densities together with reduced peak separation, indicating accelerated LiPS conversion kinetics and the introduction of additional Li^+ transport pathways.

ARTICLE IN PRESS

Quantitative kinetic analysis based on Tafel plots (**Figures 4c**, **4e-4g**, and **Figure S27**) reveals a systematic decrease in both cathodic and anodic slopes with increasing LPS content. In particular, NF-IL/LPS with 20 wt.% LPS delivers the lowest Tafel slopes (77 mV dec^{-1} for R1, 163 mV dec^{-1} for R2, and 138 mV dec^{-1} for O), reflecting substantially facilitated interfacial charge transfer. Importantly, these kinetic improvements closely follow the trends in σ and t_{Li^+}(**Figures 4c-4e**), confirming that uniformly dispersed LPS nanoparticles function beyond passive fillers. Instead, they simultaneously promote salt dissociation, provide additional Li^+ migration pathways, and suppress anion co-transport, thereby collectively enhancing redox kinetics and interfacial efficiency.[32]

Diffusion-controlled Li^+ transport was quantified by Randles-Sevcik analysis using cyclic voltammetry at variable scan rates and 60 °C (**Figures S28** and **S29**), and the extracted diffusion coefficients were compared across different electrolytes (**Figure 4i**). The PE separator exhibits the lowest peak currents and Li^+ diffusion coefficient (D_{Li^+}), whereas NF-IL shows a pronounced increase in both metrics, highlighting the effectiveness of the charged nanofiber scaffold in facilitating diffusion-controlled transport. Incorporation of LPS further enhances D_{Li^+}, with the 20 wt.% composition delivering the highest diffusivity, in good agreement with its superior σ and t_{Li^+}. However, when interfacial stability and long-term Li plating/stripping behavior at 60 °C are taken into account (**Figure S29**), NF-IL/LPS with 10 wt.% LPS emerges as the most balanced formulation, combining relatively high D_{Li^+} with the lowest polarization and robust cycling stability. Taken together, **Figures 4a-4i** demonstrate that confinement of the IL within PIL-modified nanofibers establishes a mechanically robust and electrochemically stable framework with efficient redox activity, while the introduction of LPS synergistically amplifies both charge-transfer and diffusion kinetics through its combined conductive and catalytic contributions.

ARTICLE IN PRESS

ARTICLE IN PRESS

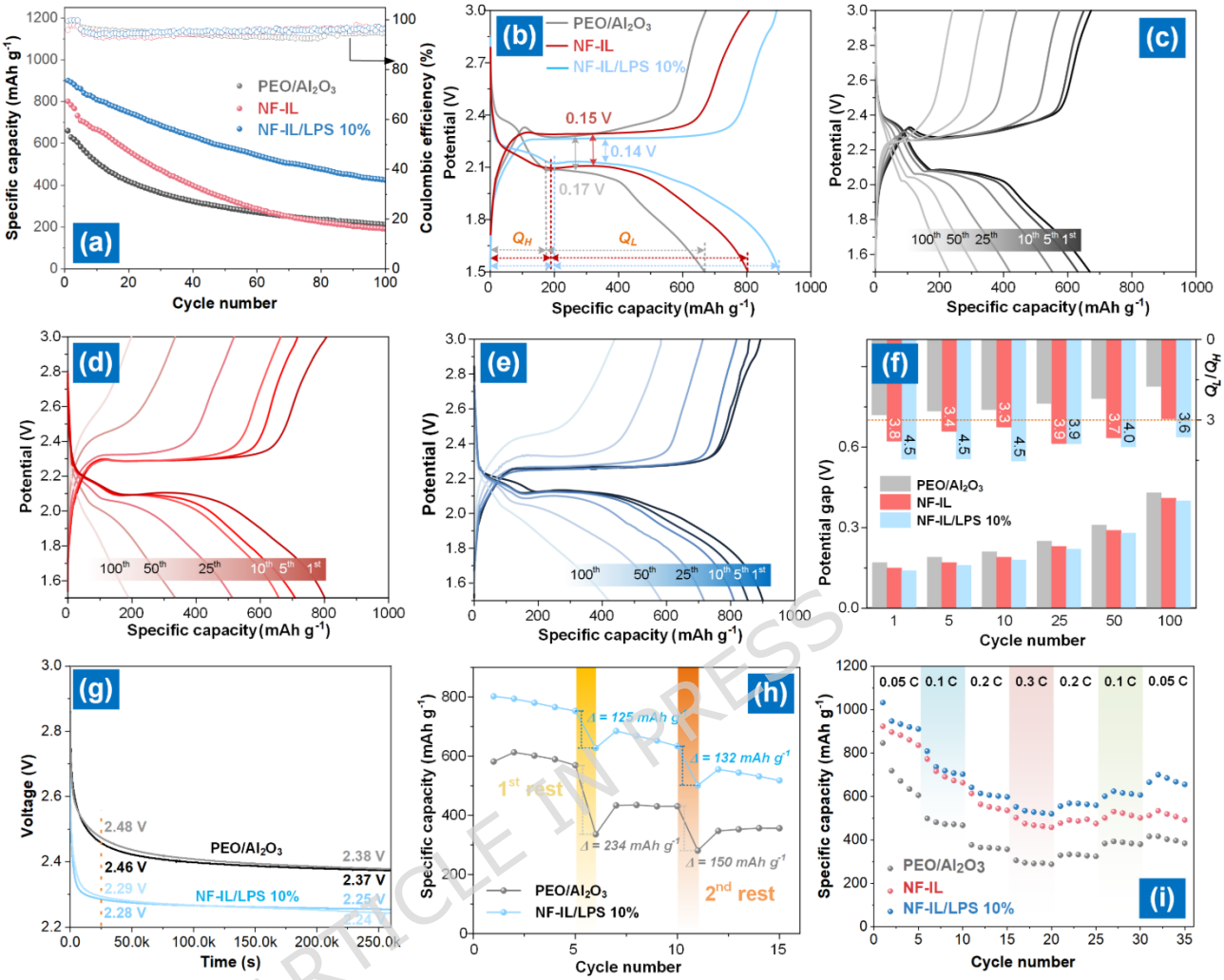

Figure 5. Electrochemical performance of Li-S cells with different CPEs at 60 °C: (a) cycling stability at 0.2 C; (b) galvanostatic charge-discharge profiles at the first cycle; galvanostatic profiles of (c) PEO/Al_2O_3, (d) NF-IL, and (e) NF-IL/LPS 10% up to the 100th cycle; (f) evolution of discharge capacity ratio (Q_L/Q_H) and potential gap; (g) voltage decay after two 72 h resting periods; (h) corresponding discharge capacities after resting; and (i) rate performance at current densities from 0.05 to 0.3 C.

Electrochemical Performance of NF-IL/LPS CPEs in Li-S Batteries

To establish a benchmark for evaluating the role of IL confinement, the electrochemical behavior of liquid-type IL-soaked separators was first examined (**Figure S30**). Both polyethylene (PE) and ANF membranes soaked with IL deliver relatively high initial capacities owing to facile ion transport; however, they suffer from rapid capacity decay at 60 °C due to aggravated LiPS shuttling and severe electrochemical polarization.[33] In sharp contrast, the NF-IL scaffold, in which the IL is confined within the PIL-modified nanofiber framework, exhibits markedly

ARTICLE IN PRESS

improved cycling stability (**Figure 5a-5e**). The reinforced architecture effectively restricts LiPS diffusion while preserving continuous and efficient Li^+ transport pathways. As shown in **Figure 5a**, PEO/Al_2O_3-based cells exhibit a low initial capacity (663 mAh g^{-1}) accompanied by rapid decay, whereas NF-IL delivers a higher initial capacity (802 mAh g^{-1}) but remains limited by insufficient long-term stability. Remarkably, NF-IL/LPS 10% combines a high discharge capacity of 903 mAh g^{-1} with reasonably stable cycling performance, maintaining 436 mAh g^{-1} after 100 cycles. The corresponding charge-discharge profiles (**Figure 5b-5e**) display well-defined voltage plateaus with substantially reduced polarization gaps, whereas the control cells progressively lose plateau integrity upon cycling. Quantitative analysis (**Figure 5f**) shows that the voltage hysteresis (ΔE) is stabilized at 0.14-0.17 V for NF-IL/LPS 10%, compared with values exceeding 0.3 V for PEO/Al_2O_3, indicating significantly mitigated polarization during cycling. Simultaneously, the Q_L/Q_H ratio exceeds the theoretical value of 3.0, reaching 3.6-3.9, which is widely regarded as a hallmark of catalytically promoted LiPS conversion rather than an effect arising solely from enhanced ionic conductivity.[34, 35]

The catalytic contribution of LPS is further supported by post-cycling SEM and impedance analyses (**Figure S31**). NF-IL exhibits pronounced interfacial resistance growth, increasing from 84 to 300 Ω, indicative of continuous interfacial degradation during repeated cycling. In contrast, NF-IL/LPS 10% shows a substantially mitigated resistance increase (26 to 215 Ω), reflecting a more stable electrode-electrolyte interface. Consistently, SEM images of cycled Li electrodes reveal a smooth and compact deposition morphology for NF-IL/LPS, whereas NF-IL suffers from porous and uneven Li growth. The restrained impedance evolution together with uniform Li morphology indicates that uniformly dispersed LPS nanoparticles not only facilitate LiPS conversion kinetics but also regulate interfacial reactions during repeated stripping/plating. To further probe the interfacial chemistry of Li metal, post-cycling XPS analysis was conducted on Li surfaces retrieved from the cells after cycling (**Figure S32**). Compared with NF-IL, the Li surface cycled with NF-IL/LPS 10% shows a significantly enhanced LiF contribution in both Li 1s and F 1s spectra, indicating the formation of a more inorganic-rich interphase. Such LiF-rich SEI layers are beneficial for stabilizing Li deposition and suppressing continuous side reactions. The S 2p spectra further reveal distinct differences in sulfur speciation. For NF-IL, clear LiPS-related terminal (S_T) and bridging (S_B) sulfur components are observed, indicating that soluble LiPS intermediates migrate to the Li surface and participate in parasitic reactions. In contrast, no detectable S_T/S_B signals are observed for NF-IL/LPS 10%, and only oxidized sulfur species (e.g., thiosulfate/polythiosulfate) are present. This result indicates that LPS effectively suppresses LiPS crossover and reduces shuttle-induced interfacial reactions at the Li metal surface. Together, these findings confirm that NF-IL/LPS stabilizes the Li/electrolyte interface through both LiF-rich SEI formation and suppression of LiPS migration. These observations demonstrate that incorporation of LPS transforms NF-IL from a purely mechanically reinforced scaffold into a bifunctional hybrid

ARTICLE IN PRESS

electrolyte that simultaneously supports efficient bulk Li^+ transport and stabilizes interfacial redox chemistry, thereby sustaining long-term cycling stability.

The tolerance of prolonged resting was further evaluated by introducing two 72 h pauses during cycling at 60 °C (**Figures 5g** and **5h**), which sensitively probes LiPS shuttle and self-discharge behavior. The PEO/Al_2O_3 cell exhibits a pronounced voltage decay (~2.37 V) accompanied by severe capacity loss (234 → 150 mAh g^{-1}), indicative of uncontrolled LiPS diffusion during rest. In contrast, NF-IL/LPS 10% maintains a higher discharge potential (~2.25 V) and even shows partial capacity recovery upon reactivation (125 → 132 mAh g^{-1}), reflecting effectively suppressed shuttle and improved reaction reversibility. This behavior is further corroborated by the preserved redox plateaus observed after resting (**Figure S33**), whereas PEO/Al_2O_3 suffers from significant plateau fading. Rate performance measurements (**Figures 5i** and **S34**) consistently support these trends: PEO/Al_2O_3 delivers the lowest capacities across all rates, while NF-IL exhibits rapid decay at elevated currents. By contrast, NF-IL/LPS 10% achieves the highest and most stable capacities of 768, 654, 532, and 421 mAh g^{-1} at 0.05, 0.1, 0.2, and 0.3 C, respectively, with full recovery upon returning to 0.05 C. The maintained discharge plateaus and reduced polarization collectively indicate that incorporation of LPS stabilizes LiPS redox dynamics and enhances transport robustness under both rest and high-rate operation, thereby mitigating self-discharge and rate-induced polarization.[36] It should be noted that the rate capability was evaluated up to 0.3 C, which is commonly adopted for solid-state Li-S systems due to transport limitations. Higher-rate performance will be further investigated in future studies.

To directly probe the interaction between LPS and lithium LiPSs, UV-vis absorption measurements were conducted using Li_2S_6 solutions before and after exposure to LPS. As shown in **Figure S35**, the characteristic absorption of Li_2S_6 significantly decreases after contact with LPS, accompanied by a clear color fading of the solution, indicating effective LiPS removal from the solution. XPS analysis (**Figure S36**) was further performed on LPS after Li_2S_6 adsorption to examine the interfacial chemical changes. In the P 2p spectrum, the main PS_4^{3-} peak shifts slightly toward higher binding energy and becomes broadened, suggesting modification of the local electronic environment of thiophosphate units. In addition, the emergence of P-O_x components indicates partial surface reconstruction during interaction with LiPSs. Meanwhile, the S 2p spectrum reveals the appearance of Li_2S_x-related sulfur species after adsorption, confirming the retention of LiPS-derived species on the LPS surface. In contrast, the high-binding-energy sulfur components assigned to oxidized species (e.g., thiosulfate/polythionate) show no obvious variation, indicating that these species are not directly involved in the adsorption process. These results demonstrate that LPS not only captures Li_2S_6 from the solution but also induces interfacial electronic interaction, supporting its role in both LiPS anchoring and conversion regulation.

ARTICLE IN PRESS

To directly assess whether LPS nanoparticles embedded within the CPE contribute to LiPS conversion, the membranes themselves were employed as the electrochemically active components, without introducing external catalysts. This configuration allows the intrinsic role of LPS to be evaluated under realistic electrolyte-working conditions. As shown in **Figure 6a**, Li_2S_6 symmetric cells assembled with NF-IL/LPS electrolytes deliver markedly higher current responses than LPS-free counterparts, indicating accelerated LiPS redox kinetics.[37] For comparison, symmetric cell measurements were also conducted using NF-IL/LPS (10 wt.%). Although the current response is lower than that of the 30 wt.% sample, the redox peaks exhibit improved symmetry and stability. This behavior is attributed to more uniform dispersion of LPS nanoparticles at lower loading, which promotes homogeneous interfacial reactions and reduces localized polarization. These results suggest that while higher LPS content enhances catalytic activity, excessive loading may disrupt structural homogeneity and ion-transport pathways, leading to suboptimal electrochemical performance. Consistently, Li_2S_8 nucleation measurements (**Figures 6b** and **6c**) show increased nucleation current densities and larger Li_2S deposition capacities for NF-IL/LPS, reflecting faster nucleation and more complete LiPS conversion. These results demonstrate that LPS plays a dual role within the electrolyte, simultaneously facilitating Li^+ transport and promoting interfacial LiPS redox reactions.[38]

Transport kinetics were further evaluated by galvanostatic intermittent titration technique at 60 °C (GITT, **Figures 6d** and **6e**). NF-IL/LPS 10% exhibits larger potential steps and shorter relaxation times compared with NF-IL and PEO/Al_2O_3, corresponding to higher apparent Li^+ diffusion coefficients. The corresponding IR-drop analysis (**Figure 6e**) reveals reduced polarization in the presence of LPS, indicative of improved interfacial charge-transfer behavior. The extracted diffusion coefficients and decreased overpotentials (**Figure 6f**) collectively indicate that LPS contributes dual functions within the electrolyte, providing additional Li^+ migration pathways while facilitating LiPS redox processes.[39] Together, these results demonstrate that LPS incorporation not only reinforces mechanical integrity and bulk ionic transport, but also promotes favorable interfacial kinetics, thereby underpinning the enhanced electrochemical stability observed in **Figure 5**.

To further elucidate the role of LPS in regulating LiPS redox processes, XPS spectra were collected at two representative discharge states, point B (intermediate plateau) and point E (end of discharge) (**Figures 6g** and **6h**). At point B, corresponding to the conversion of long-chain LiPSs (Li_2S_6/Li_2S_8) into shorter-chain species (Li_2S_4), the ratio of bridging sulfur (S_B) to terminal sulfur (S_T) (S_B/S_T) is commonly used as an indicator of conversion progress. In PEO/Al_2O_3, a relatively high S_b/S_t ratio suggests the accumulation of intermediate LiPSs, whereas NF-IL/LPS 10% exhibits a markedly reduced S_b/S_t ratio, reflecting facilitated S-S bond cleavage and more efficient progression toward short-chain species. At point E, corresponding to the final reduction into insoluble Li_2S_2/Li_2S, NF-IL/LPS 10%

displays substantially attenuated sulfur-related signals compared with PEO/Al_2O_3, indicating a more complete conversion with fewer residual sulfur species remaining on the cathode surface.[40, 41] Collectively, these results indicate that LPS incorporation promotes both the forward conversion of long-chain LiPSs and the subsequent reduction to Li_2S, thereby suppressing intermediate accumulation and enabling a more complete sulfur redox process, which is consistent with adsorption behavior (**Figures S35** and **S36**).

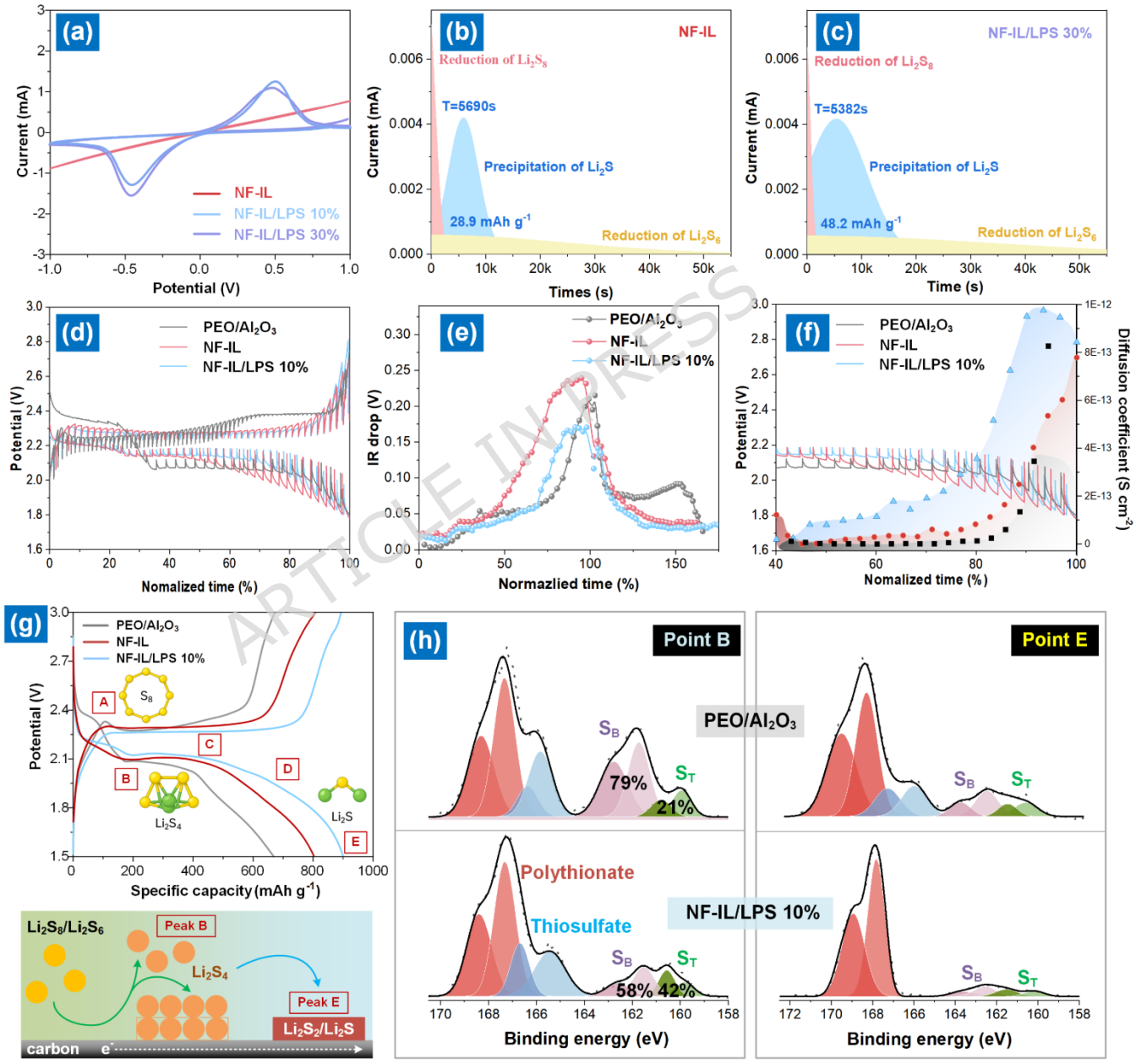

Figure 6. (a) Symmetric cell tests with Li_2S_6 catholyte demonstrating catalytic activity of NF-IL, NF-IL/LPS 10% and 30%. Li_2S_8 nucleation profiles for (b) NF-IL

ARTICLE IN PRESS

and (c) NF-IL/LPS 30%. (d) GITT curves of cells with PEO/Al_2O_3, NF-IL, and NF-IL/LPS 10%. Corresponding (e) IR drop and (f) calculated Li^+ diffusion coefficients. (g) Charge-discharge profiles at 0.1 C and schematic of sulfur redox processes at different states (A-E). (h) Ex-situ S 2p XPS of electrodes at point B and E, highlighting differences in sulfur species evolution.

To gain atomic-level insight into the interaction between LPS and LiPS species, DFT calculations were performed (**Figure 7a**). The calculated adsorption energies (**Figure 7b**) show that short-chain intermediates (Li_2S_4, Li_2S_2, and Li_2S) bind more strongly to LPS surfaces than long-chain Li_2S_6/Li_2S_8 or elemental S_8. Such preferential adsorption is expected to suppress LiPS dissolution while promoting their retention and subsequent conversion at the electrolyte interface.[42] The corresponding free-energy diagram (**Figure 7c**) indicates a thermodynamically favorable reduction pathway from S_8* to Li_2S*, with pronounced stabilization of Li_2S_4 and Li_2S_2 intermediates. This behavior contrasts with conventional carbonaceous or oxide hosts, which typically exhibit weaker adsorption and higher energetic penalties for the $Li_2S_4 \rightarrow Li_2S$ conversion step.[43] The enhanced stabilization arises from the dual characteristics of LPS, where polar PS_4^{3-} units provide strong chemical affinity toward LiPSs, while mobile Li^+ species facilitate local ionic compensation, collectively lowering the energetic barriers for multistep sulfur reduction.

These theoretical insights are consistent with the electrochemical observations, including higher nucleation currents and increased Li_2S deposition capacities (**Figures 6b** and **6c**), reduced residual sulfur species at the end-of-discharge state (**Figure 6h**), and narrowed voltage polarization accompanied by elevated Q_L/Q_H ratios exceeding 3 (**Figure 5f**).[44] Together, these results indicate that embedded LPS nanoparticles not only enhance ionic transport within the composite electrolyte but also actively participate in regulating LiPS conversion by lowering the energetic barriers associated with sulfur reduction. As schematically illustrated in **Figure 7d**, the cooperative effects of LPS-assisted ion hopping, interfacial conversion promotion, and stabilized Li deposition collectively establish a robust electrochemical environment, accounting for the improved cycling stability and rate performance of NF-IL/LPS CPEs. These mechanistic insights establish a clear structure-property-performance correlation for the NF-IL/LPS design, consistent with the electrochemical performance observed in Li-S cells. These mechanistic insights establish a clear structure-property-performance correlation for the NF-IL/LPS design, consistent with the electrochemical performance observed in Li-S cells. To further contextualize the present system, a comparison with representative solid polymer and CPEs for Li-S batteries is summarized in **Table S1**. As shown, previously reported systems primarily focus on improving individual aspects of electrolyte performance, such as enhancing s through filler incorporation, increasing $\square_{Li^+}$ *via* polymer design, or stabilizing interfaces through surface engineering. In contrast, the NF-IL/LPS electrolyte uniquely integrates a nanofiber scaffold, IL phase, and sulfide fillers, enabling a dual-pathway Li^+ transport mechanism together with catalytic regulation of LiPS conversion. This synergistic design allows simultaneous optimization of ionic transport, interfacial stability, and

ARTICLE IN PRESS

sulfur redox kinetics, which is rarely achieved in conventional composite polymer electrolytes.

Conclusion

In conclusion, we have developed a nanofiber-constructed CPE by integrating PIL-modified aramid nanofibers with sulfide-based Li_3PS_4 nanoparticles, providing a unified solution to the long-standing challenges of mechanical robustness, ion transport, and LiPS regulation in Li-S batteries. The PIL coating stabilizes the aramid nanofiber network and establishes continuous surface-assisted pathways for long-range Li^+ diffusion, while Li_3PS_4 introduces polarized N/S/O coordination environments that create sulfide-rich interfacial hopping sites and catalytically regulate LiPS conversion. This synergistic dual-mode transport mechanism, combining framework-mediated diffusion with localized interfacial hopping, endows the hybrid electrolyte with high ionic conductivity, an elevated Li^+ transference number, and durable interfacial stability. Consequently, Li-S cells assembled with this electrolyte exhibit high reversible capacity, excellent Coulombic efficiency, and robust rate capability under elevated-temperature operation. More broadly, this work demonstrates a generalizable composite-electrolyte design strategy that integrates mechanically resilient nanofiber frameworks with catalytically active ionic fillers, offering a versatile platform for bridging liquid-like ion mobility with solid-like stability in next-generation high-energy rechargeable batteries.

ARTICLE IN PRESS

ARTICLE IN PRESS

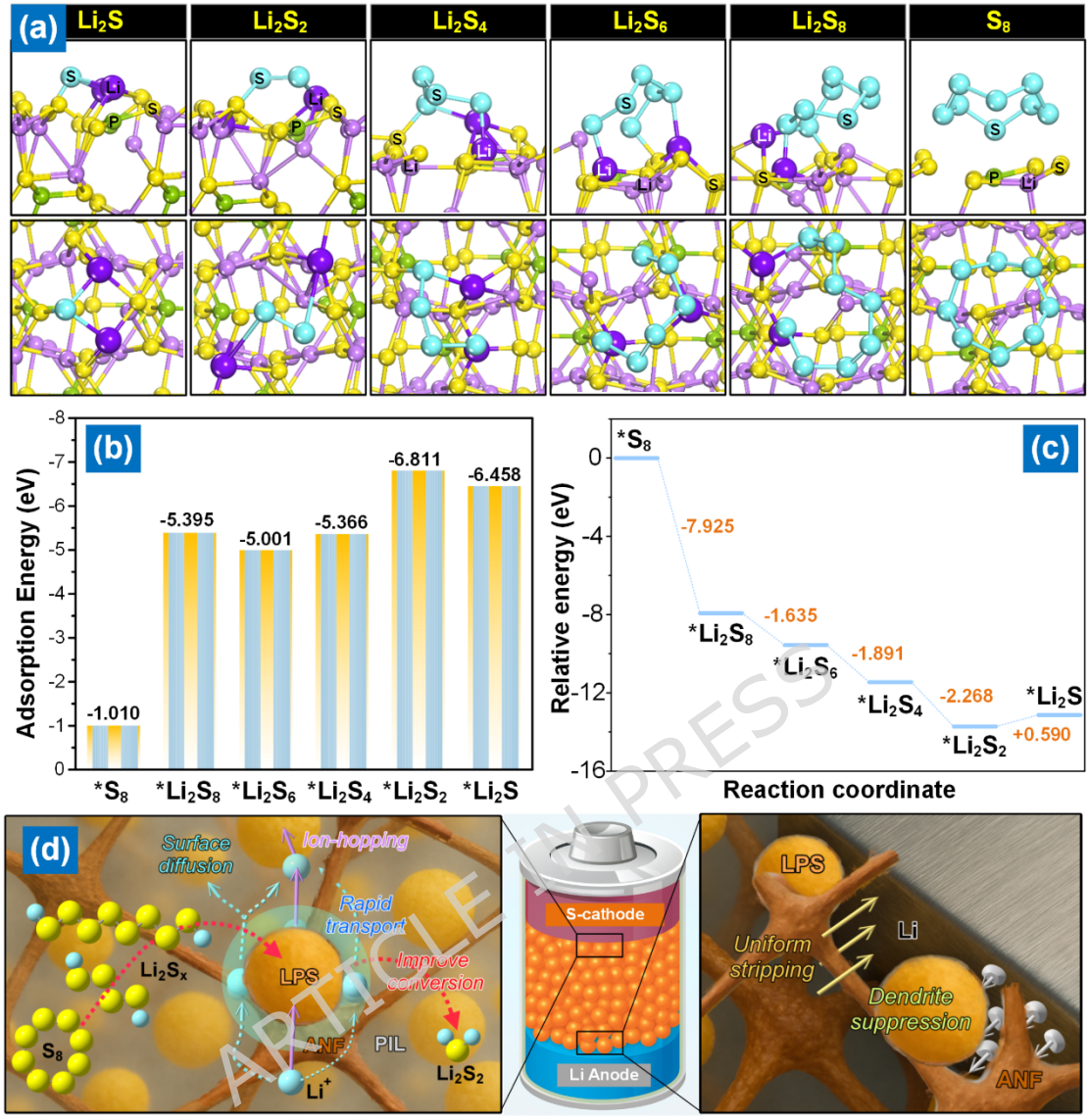

Figure 7. DFT analysis of the catalytic role of LPS fillers. (a) Optimized adsorption configurations of S_8 and Li_2S_x species. (b) Adsorption energies showing stronger binding with Li_2S_x intermediates. (c) Free-energy pathway illustrating reduced barriers for Li_2S formation. (d) Schematic mechanism: LPS fillers facilitate LiPS conversion, promote uniform Li deposition, and stabilize Li^+ transport within the PIL@ANF framework.

Supporting Information

Supporting Information is available from the Springer Nature platform. It contains detailed experimental procedures, supplementary FTIR, XPS, XRD, SEM/TEM, and FIB-EDS analyses, extended electrochemical characterizations (including LSV, EIS, GITT, and Li^+ transference number measurements), LiPS conversion tests, and computational details for DFT and molecular dynamics simulations.

Acknowledgements

ARTICLE IN PRESS

The authors acknowledge analytical and technical support from the Instrumentation Center at National Sun Yat-sen University. The authors also thank Dr. Shing-Jong Huang (Instrumentation Center, National Taiwan University) for assistance with the 600 MHz solid-state NMR measurements.

Funding

This work was supported by the National Science and Technology Council (NSTC), Taiwan, under Grant Nos. 114-2221-E-110-009-MY3, 114-2622-E-110-022- and 114-2639-E-011-001-ASP.

Author Contributions

C.Y. Kuo conducted material synthesis, experimental characterization, data analysis, and carried out the main research work. **W. M. Huang** and **J. Y. Li.** assisted with electrochemical testing and data analysis. **M. G. Mohamed** assisted with structural testing and data analysis. **S. W. Kuo** provided technical support for materials characterization. **C. H. Huang** provided technical support for materials characterization. **B. J. Hwang** contributed to experimental support and funding acquisition. **Y. S. Ye** conceived and designed the study, performed data interpretation, wrote the manuscript, and acquired research funding. All authors discussed the results and approved the final manuscript.

References

[1] S. Yari, A. Conde Reis, Q. Pang, M. Safari, Performance benchmarking and analysis of lithium-sulfur batteries for next-generation cell design, Nature Communications 16(1) (2025) 5473. https://doi.org/10.1038/s41467-025-60528-4.
[2] Z. Song, F. Chen, M. Martinez-Ibañez, W. Feng, M. Forsyth, Z. Zhou, M. Armand, H. Zhang, A reflection on polymer electrolytes for solid-state lithium metal batteries, Nature Communications 14(1) (2023) 4884. https://doi.org/10.1038/s41467-023-40609-y.
[3] J. Grill, S.K. Steensen, D.L.Q. Castro, I.E. Castelli, J. Popovic-Neuber, Solid-state inorganic electrolytes for next generation potassium batteries, Communications Materials 5(1) (2024) 127. https://doi.org/10.1038/s43246-024-00568-3.
[4] D. Wang, L.J. Jhang, R. Kou, M. Liao, S. Zheng, H. Jiang, P. Shi, G.X. Li, K. Meng, D. Wang, Realizing high-capacity all-solid-state lithium-sulfur batteries using a low-density inorganic solid-state electrolyte, Nat Commun 14(1) (2023) 1895. https://doi.org/10.1038/s41467-023-37564-z.
[5] X. Lu, Y. Wang, X. Xu, B. Yan, T. Wu, L. Lu, Polymer-Based Solid-State Electrolytes for High-Energy-Density Lithium-Ion Batteries – Review, Advanced Energy Materials 13(38) (2023) 2301746. https://doi.org/https://doi.org/10.1002/aenm.202301746.
[6] Y. Kim, W.I. Kim, H. Park, J.S. Kim, H. Cho, J.S. Yeon, J. Kim, Y.-J. Kim, J. Lee, H.S. Park, Multifunctional Polymeric Phthalocyanine-Coated Carbon Nanotubes for Efficient Redox Mediators of Lithium–Sulfur Batteries, Advanced Energy Materials 13(22) (2023) 2204353.

ARTICLE IN PRESS

https://doi.org/https://doi.org/10.1002/aenm.202204353.
[7] M. Jana, R. Xu, X.-B. Cheng, J.S. Yeon, J.M. Park, J.-Q. Huang, Q. Zhang, H.S. Park, Rational design of two-dimensional nanomaterials for lithium–sulfur batteries, Energy & Environmental Science 13(4) (2020) 1049-1075. https://doi.org/10.1039/C9EE02049G.
[8] W.I. Kim, J.C. Shin, M.J. Kim, G. Jang, M. Lee, H.S. Park, Ionic Structured Redox-Mediating Polymeric Sulfurs for Lithium–Sulfur Batteries, ACS Energy Letters 10(5) (2025) 2410-2418. https://doi.org/10.1021/acsenergylett.5c00808.
[9] S. Li, L. Li, H. Yang, Y. Zhao, Y. Shan, A review of composite polymer electrolytes for solid-state lithium-sulfur batteries: Synthesis methods, optimal design, and critical challenges, Chemical Engineering Journal 484 (2024) 149433. https://doi.org/https://doi.org/10.1016/j.cej.2024.149433.
[10] B. Tao, D. Zhong, H. Li, G. Wang, H. Chang, Halide solid-state electrolytes for all-solid-state batteries: structural design, synthesis, environmental stability, interface optimization and challenges, Chemical Science 14(33) (2023) 8693-8722. https://doi.org/10.1039/D3SC02093B.
[11] Z. Chen, J. Hou, M. Yang, J. Zhu, X. Zhuang, Sulfide-based solid electrolyte and electrode membranes for all-solid-state lithium batteries, Chemical Engineering Journal 502 (2024) 158136. https://doi.org/https://doi.org/10.1016/j.cej.2024.158136.
[12] Z. Li, J. Fu, X. Zhou, S. Gui, L. Wei, H. Yang, H. Li, X. Guo, Ionic Conduction in Polymer-Based Solid Electrolytes, Advanced Science 10(10) (2023) 2201718. https://doi.org/https://doi.org/10.1002/advs.202201718.
[13] X. Wang, L. Ye, C.-W. Nan, X. Li, Effect of Solvents on a Li10GeP2S12-Based Composite Electrolyte via Solution Method for Solid-State Battery Applications, ACS Applied Materials & Interfaces 14(41) (2022) 46627-46634. https://doi.org/10.1021/acsami.2c12920.
[14] K.T. Kim, D.Y. Oh, S. Jun, Y.B. Song, T.Y. Kwon, Y. Han, Y.S. Jung, Tailoring Slurries Using Cosolvents and Li Salt Targeting Practical All-Solid-State Batteries Employing Sulfide Solid Electrolytes, Advanced Energy Materials 11(17) (2021) 2003766. https://doi.org/https://doi.org/10.1002/aenm.202003766.
[15] Z. Li, J. Miao, W. Hu, Y. Liu, M. Li, M. Zhao, J. Liu, L. Xiao, Stabilizing the oxide cathode/sulfide solid electrolyte interface via a novel polyaniline coating prepared by ball milling, Chemical Communications 59(37) (2023) 5627-5630. https://doi.org/10.1039/D3CC00722G.
[16] Y. Wang, J. Ju, S. Dong, Y. Yan, F. Jiang, L. Cui, Q. Wang, X. Han, G. Cui, Facile Design of Sulfide-Based all Solid-State Lithium Metal Battery: In Situ Polymerization within Self-Supported Porous Argyrodite Skeleton, Advanced Functional Materials 31(28) (2021) 2101523. https://doi.org/https://doi.org/10.1002/adfm.202101523.
[17] K.-S. Oh, J.E. Lee, Y.-H. Lee, Y.-S. Jeong, I. Kristanto, H.-S. Min, S.-M. Kim, Y.J. Hong, S.K. Kwak, S.-Y. Lee, Elucidating Ion Transport Phenomena in Sulfide/Polymer Composite Electrolytes for Practical Solid-State Batteries, Nano-Micro Letters 15(1) (2023) 179. https://doi.org/10.1007/s40820-023-

ARTICLE IN PRESS

01139-w.
[18] G.G. Serbessa, B.W. Taklu, Y. Nikodimos, N.T. Temesgen, Z.B. Muche, S.K. Merso, T.-I. Yeh, Y.-J. Liu, W.-S. Liao, C.-H. Wang, S.-H. Wu, W.-N. Su, C.-C. Yang, B.J. Hwang, Boosting the Interfacial Stability of the Li6PS5Cl Electrolyte with a Li Anode via In Situ Formation of a LiF-Rich SEI Layer and a Ductile Sulfide Composite Solid Electrolyte, ACS Applied Materials & Interfaces 16(8) (2024) 10832-10844. https://doi.org/10.1021/acsami.3c14763.
[19] H. Pei, C. Yang, Q. Wu, X. Zhou, X. Xie, B. Hwang, Y. Ye, Ion-selective aramid nanofiber-based Janus separators fabricated by a dry-wet phase inversion approach for lithium–sulfur batteries, Journal of Materials Chemistry A 10(10) (2022) 5317-5327. https://doi.org/10.1039/D1TA09533A.
[20] S.-O. Tung, S. Ho, M. Yang, R. Zhang, N.A. Kotov, A dendrite-suppressing composite ion conductor from aramid nanofibres, Nature Communications 6(1) (2015) 6152. https://doi.org/10.1038/ncomms7152.
[21] M. Yang, K. Cao, L. Sui, Y. Qi, J. Zhu, A. Waas, E.M. Arruda, J. Kieffer, M.D. Thouless, N.A. Kotov, Dispersions of Aramid Nanofibers: A New Nanoscale Building Block, ACS Nano 5(9) (2011) 6945-6954. https://doi.org/10.1021/nn2014003.
[22] B. Liu, Y. Chen, Q. Zhang, Y. Lai, R. Lin, L. Luo, J. Lv, X. Liu, Abnormal High-Temperature-Enhanced Hydrogen Bond-Related π–π Hybrid Interaction in Heterocyclic Aramid Fiber-Assisted Chain Self-Ordering, Macromolecules 58(14) (2025) 7104-7111. https://doi.org/10.1021/acs.macromol.5c00889.
[23] E.C. Self, Z.D. Hood, T. Brahmbhatt, F.M. Delnick, H.M. Meyer, III, G. Yang, J.L.M. Rupp, J. Nanda, Solvent-Mediated Synthesis of Amorphous Li3PS4/Polyethylene Oxide Composite Solid Electrolytes with High Li+ Conductivity, Chemistry of Materials 32(20) (2020) 8789-8797. https://doi.org/10.1021/acs.chemmater.0c01990.
[24] Y. Nikodimos, C.-j. Huang, B.W. Taklu, W.-N. Su, B.J. Hwang, Chemical stability of sulfide solid-state electrolytes: stability toward humid air and compatibility with solvents and binders, Energy & Environmental Science 15(3) (2022) 991-1033. https://doi.org/10.1039/D1EE03032A.
[25] L. Si, Y. Wu, H. Xiao, W. Xing, R. Song, Y. Li, S. Wang, X. Liang, W. Yu, J. Song, S. Shen, A superstable, flexible, and scalable nanofluidic ion regulation composite membrane, Science Bulletin 68(20) (2023) 2344-2353. https://doi.org/https://doi.org/10.1016/j.scib.2023.08.060.
[26] E. Darnbrough, J. Aspinall, M. Pasta, D.E.J. Armstrong, Elastic and plastic mechanical properties of lithium measured by nanoindentation, Materials & Design 233 (2023) 112200. https://doi.org/https://doi.org/10.1016/j.matdes.2023.112200.
[27] X. Yang, J. Liu, N. Pei, Z. Chen, R. Li, L. Fu, P. Zhang, J. Zhao, The Critical Role of Fillers in Composite Polymer Electrolytes for Lithium Battery, Nanomicro Lett 15(1) (2023) 74. https://doi.org/10.1007/s40820-023-01051-3.
[28] X. Yu, L. Zhao, Y. Li, Y. Jin, D.J. Politis, H. Liu, H. Wang, M. Liu, Y.-B. He, L. Wang, Weakening Ionic Coordination for High Ionic Conductivity Composite Solid Electrolytes, ACS Energy Letters 9(5) (2024) 2109-2115. https://doi.org/10.1021/acsenergylett.4c00636.

ARTICLE IN PRESS

ARTICLE IN PRESS

[29] H. Stöffler, T. Zinkevich, M. Yavuz, A. Senyshyn, J. Kulisch, P. Hartmann, T. Adermann, S. Randau, F.H. Richter, J. Janek, S. Indris, H. Ehrenberg, Li+-Ion Dynamics in β-Li3PS4 Observed by NMR: Local Hopping and Long-Range Transport, The Journal of Physical Chemistry C 122(28) (2018) 15954-15965. https://doi.org/10.1021/acs.jpcc.8b05431.
[30] S. Liu, L. Zhou, T. Zhong, X. Wu, K. Neyts, Sulfide/Polymer Composite Solid-State Electrolytes for All-Solid-State Lithium Batteries, Advanced Energy Materials 14(48) (2024) 2403602. https://doi.org/https://doi.org/10.1002/aenm.202403602.
[31] P. Ghorbanzade, A. Pesce, M. Armand, K. Gómez, S. Devaraj, P. López-Aranguren, J.M. López del Amo, Unveiling the Reactivity and the Li-Ion Exchange at the PEO-Li6PS5Cl Interphase: Insights from Solid-State NMR, Small Structures 5(10) (2024) 2400139. https://doi.org/https://doi.org/10.1002/sstr.202400139.
[32] J. Fu, Z. Li, X. Zhou, X. Guo, Ion transport in composite polymer electrolytes, Materials Advances 3(9) (2022) 3809-3819. https://doi.org/10.1039/D2MA00215A.
[33] H.J. Pei, C.Y. Yang, P.P. Wang, J.Y. Lin, L.L. Yin, X.P. Zhou, X.L. Xie, Y.S. Ye, Efficient thermal management of lithium-sulfur batteries by highly thermally conductive LBL-assembled composite separators, Electrochimica Acta 407 (2022) 139807. https://doi.org/ARTN 139807

10.1016/j.electacta.2021.139807.
[34] H. Park, J. Lee, C. Yu, Facilitating polysulfide conversion kinetics via multifunctional solid-state electrolytes under lean electrolyte conditions for lithium–sulfur batteries, Journal of Materials Chemistry A 13(6) (2025) 4452-4459. https://doi.org/10.1039/D4TA07639G.
[35] H. Li, X. Wang, H. Ma, D. Guo, L. Wu, H. Jin, X.a. Chen, S. Wang, A Review on Catalytic Progress of Polysulfide Redox Reactions on Transition Metal Sulfides in Li-S Batteries from Structural Perspective, ChemElectroChem 11(10) (2024) e202300696. https://doi.org/https://doi.org/10.1002/celc.202300696.
[36] H. Xu, Q. Jiang, K.S. Hui, S. Wang, L. Liu, T. Chen, Y. Zheng, W.F. Ip, D.A. Dinh, C. Zha, Z. Lin, K.N. Hui, Interfacial “Double-Terminal Binding Sites” Catalysts Synergistically Boosting the Electrocatalytic Li2S Redox for Durable Lithium–Sulfur Batteries, ACS Nano 18(12) (2024) 8839-8852. https://doi.org/10.1021/acsnano.3c11903.
[37] Y.S. Ye, M.G. Mohamed, N.H. Ye, T.Y. Hung, G.Y. Chen, S.H. Lin, M.C. Tsai, B.J. Hwang, S.W. Kuo, Single-Atom Catalyst-Integrated Porous Organic Polymers for High-Performance Lithium-Sulfur Batteries, Small 21(32) (2025) e2503250. https://doi.org/10.1002/smll.202503250.
[38] H. Yang, L. Wang, C. Geng, Y. Zhao, Q. Li, X. Jiang, Z. Tian, M. Wang, C. Jiang, Z. Sun, B. Cui, Y.-B. He, W. Chen, W. Lv, Q.-H. Yang, Catalytic Solid-State Sulfur Conversion Confined in Micropores toward Superhigh Coulombic Efficiency Lithium-Sulfur Batteries, Advanced Energy Materials 14(21) (2024) 2400249. https://doi.org/https://doi.org/10.1002/aenm.202400249.
[39] H. Kim, H.-N. Choi, J.-Y. Hwang, C.S. Yoon, Y.-K. Sun, Tailoring the Interface

ARTICLE IN PRESS

between Sulfur and Sulfide Solid Electrolyte for High-Areal-Capacity All-Solid-State Lithium–Sulfur Batteries, ACS Energy Letters 8(10) (2023) 3971-3979. https://doi.org/10.1021/acsenergylett.3c01473.
[40] W. Sun, S. Liu, Y. Li, D. Wang, Q. Guo, X. Hong, K. Xie, Z. Ma, C. Zheng, S. Xiong, Monodispersed FeS2 Electrocatalyst Anchored to Nitrogen-Doped Carbon Host for Lithium–Sulfur Batteries, Advanced Functional Materials 32(43) (2022) 2205471. https://doi.org/https://doi.org/10.1002/adfm.202205471.
[41] K. Chen, Y. Zhu, Z. Huang, B. Han, Q. Xu, X. Fang, J. Xu, Strengthened d–p Orbital Hybridization on Metastable Cubic Mo2C for Highly Stable Lithium–Sulfur Batteries, ACS Nano 18(51) (2024) 34791-34802. https://doi.org/10.1021/acsnano.4c11701.
[42] W. Hua, H. Li, C. Pei, J. Xia, Y. Sun, C. Zhang, W. Lv, Y. Tao, Y. Jiao, B. Zhang, S.-Z. Qiao, Y. Wan, Q.-H. Yang, Selective Catalysis Remedies Polysulfide Shuttling in Lithium-Sulfur Batteries, Advanced Materials 33(38) (2021) 2101006. https://doi.org/https://doi.org/10.1002/adma.202101006.
[43] Y. Huang, L. Lin, C. Zhang, L. Liu, Y. Li, Z. Qiao, J. Lin, Q. Wei, L. Wang, Q. Xie, D.-L. Peng, Recent Advances and Strategies toward Polysulfides Shuttle Inhibition for High-Performance Li–S Batteries, Advanced Science 9(12) (2022) 2106004. https://doi.org/https://doi.org/10.1002/advs.202106004.
[44] Y. Shen, T. Pan, L. Wang, Z. Ren, W. Zhang, F. Huo, Programmable Logic in Metal–Organic Frameworks for Catalysis, Advanced Materials 33(46) (2021) 2007442. https://doi.org/https://doi.org/10.1002/adma.202007442.

ARTICLE IN PRESS